actuators

MDPI

Article

Designing a Robotic Gripper Based on the Actuating Capacity of NiTi-Based Shape Memory Wires

Adrian Petru Teodoriu [1], Bogdan Pricop [1], Nicoleta-Monica Lohan [1], Mihai Popa [1], Radu Ioachim Comăneci [1], Ioan Doroftei [1,2] and Leandru-Gheorghe Bujoreanu [1,*]

[1] Faculty of Materials Science, "Gheorghe Asachi" Technical University of Iasi, Blvd. D. Mangeron 41, 700050 Iasi, Romania; nicoleta-monica.lohan@academic.tuiasi.ro (N.-M.L.)
[2] Romanian Academy of Technical Sciences, 26 Dacia Blvd., 030167 Bucharest, Romania
* Correspondence: leandru-gheorghe.bujoreanu@academic.tuiasi.ro

Abstract: In the present study, the capacity of two commercial NiTi and NiTiCu shape memory alloy (SMA) wires to develop work-generating (WG) and constrained-recovery (CR) shape memory effects (SMEs), as well as the capacity of a commercial NiTiFe super-elastic wire to act as cold-shape restoring element, have been investigated. Using differential scanning calorimetry (DSC), the reversible martensitic transformation to austenite of the three NiTi-based wires under study was emphasized by means of an endothermic minimum of the heat flow variation with temperature. NiTi and NiTiCu wire fragments were further tested for both WG-SME and CR-SME developed during the heating, from room temperature (RT) to different maximum temperatures selected from the DSC thermograms. The former tests revealed the capacity to repetitively lift various loads during repetitive heating, while the latter tests disclosed the repetitive development of shrinkage stresses during the repetitive heating of elongated wires. The tensile behavior of the three NiTi-based SMA wires was analyzed by failure and loading–unloading tests. The study disclosed the actuation capacity of NiTi and NiTiCu shape memory wires, which were able to develop work while being heated, as well as the resetting capacity of NiTiFe super-elastic wires, which can restore the initial undeformed shape of shape memory wires which soften while being cooled down. These features enable the design of a robotic gripper based on the development of NiTi-based actuators with repetitive action.

Keywords: shape memory alloy; super-elastic alloy; martensitic transformation; work; constrained recovery; repetitive actuation

check for updates

Citation: Teodoriu, A.P.; Pricop, B.; Lohan, N.-M.; Popa, M.; Comăneci, R.I.; Doroftei, I.; Bujoreanu, L.-G. Designing a Robotic Gripper Based on the Actuating Capacity of NiTi-Based Shape Memory Wires. *Actuators* **2024**, *13*, 319. https://doi.org/10.3390/act13080319

Academic Editor: Giulia Scalet

Received: 3 July 2024
Revised: 14 August 2024
Accepted: 18 August 2024
Published: 21 August 2024

Copyright: © 2024 by the authors. Licensee MDPI, Basel, Switzerland. This article is an open access article distributed under the terms and conditions of the Creative Commons Attribution (CC BY) license (https://creativecommons.org/licenses/by/4.0/).

1. Introduction

Shape memory alloys (SMAs) are able to recover a "hot shape", which was induced in the austenite high-temperature state, by simply heating an element to which a "cold shape" was induced in the martensite low-temperature state. [1] This heating-triggered phenomenon is called shape memory effect (SME) and can be observed in alloys, ceramics and polymers [2]. Depending on the constraints that the SMA has to overcome during its hot shaped recovery, SME can be: (i) with free recovery (FR) without constraints, (ii) with constrained recovery (CR) with stress development at a constant strain, or (iii) work generating (WG) with stroke development under a constant force [3].

The work generating capacity of SMAs inspired the first exposure of an application of these materials at the Brussels International Fair in 1958. It was a cycling lifting device actuated by an Au-Cd single crystal which lifted a load during electrical resistive heating and lowered it back during air-fan cooling. This was the first ever mentioned SMA-activated thermal actuator [4].

With the discovery of NiTi SMA in 1963 [5], a remarkable burst in the development of actuators with active elements made from NiTi-based SMAs was observed [6]. This progress was enhanced by the advance of ternary alloyed NiTi-based SMAs, such as Ni-Ti-Cu or Ni-Ti-Fe [7]. The former has been able to decrease transformation hysteresis, stabilize critical

transformation temperature, soften the martensite, and cause a two-step shape change [8]. The latter depressed the critical temperatures of the martensitic transformation below room temperature (RT) which enabled the alloys to be austenitic at RT [9]. Some SMAs experience a reversible thermoelastic martensitic transformation which is the mechanism of a work-generating SME [10]. These commercial SMAs, based on NiTi, CuZnAl, or CuAlNi, when deformed in an austenitic state, enable the obtainment of an unstable stress-induced martensite which forms during loading and reverts to austenite during unloading. This mechanism governs super-elasticity (SE) behavior, characterized by RT unloading recovery strains that, in special cases, can be as high as 25% [11].

NiTi-based SMAs have been produced in the form of wires [12], beams [13], coil [14] or helical springs [15], thin plates [16], etc., which can provide various useful properties [17]. One of these properties is the quiet and soft operation that enabled the development of various bioinspired applications, mimicking the operation of the tendons, such as robotic arms capable of pan–tilt movements [18]. By connecting several NiTi wires in series, large values for specific strokes and work outputs were obtained at a parallel gripper [19].

NiTi-based SMAs have a remarkable storage capacity, releasing as much as 4 J/g upon heating-induced SME and 6.5 J/g during super-elastic RT unloading [20]. Based on these features, a large variety of work-generating SME-driven applications have been fabricated [21], such as mini modular mechanical devices [22], small bioinspired robots [23], self-sensing compact actuators [24], artificial limbs [25], and dynamic vibration absorbers [26]. These applications are generally characterized by a long functional fatigue life, being able to withstand up to 10^5 cycles [27].

One of the main drawbacks of all SMA-driven actuators is the requirement of "cold shape" resetting, since the material is unable to develop a perceptible amount of work during cooling [28]. A possible solution could be the application of a training thermomechanical treatment meant to obtain two-way shape memory effects (TWSME). Through TWSME, the active SMA element can instantly recover its hot shape during heating and its cold shape during cooling [29]. Various training procedures have been devised, such as the bidirectional memory effect training method, which enables maximum deflections of about 10 mm [30]. Nevertheless, due to some structural and functional fatigue phenomena, both hot and cold shapes become gradually deformed, as compared to the initial ones, and the total stroke is reduced [31].

Other constructive solutions involved the use of "dead loads" that diminish the useful stroke developed by WG-SME during heating and have the merit of resetting the cold shape, thus enhancing the cycling functioning of the actuator [32].

Several constructive variants have been adopted for "cold shape" resetting. The first variant was the use of regular steel springs which had the disadvantage of producing the maximum resetting force at the beginning of the backstroke [6]. The improved variants involved using reciprocating SMA elements [33] or a pair formed by an SMA and a super-elastic element [34]. The functioning principle of the SMA/super-elastic coupling consists in the deformation of the latter during the heating of the former (that becomes tougher during heating and softer during cooling) and its shape resetting under the effect of the super-elastic element that forces it to recover its cold shape [35].

Based on the actuation capacity of NiTi-based SMAs, several types of grippers were developed. Some representative examples include a soft robotic gripper capable of handling delicate things [36], a module with adjustable grasping stiffness [37], or a modular soft gripper driven by large wire tendons [38].

A particular type of solution was introduced by Guo et al., who designed a compliant differential SMA actuator with two antagonistic wires, coupled by a torsion steel spring, that developed an angular motion [39].

All these applications have their specific disadvantages concerning cold shape resetting. The use of bias steel springs caused an increase in the resistance force with the increase in the stroke, while the backstroke is subjected to maximum resetting force at the beginning. On the other hand, using SMA/super-elastic couplings did not involve a direct connection

between the two executive elements, which caused an efficiency loss from an energetic point of view.

The present paper aims to: (i) evaluate the capacities of NiTi-based SMAs to develop WG and CR-SME as well as to accommodate tensile strains both during single and multiple cycling); (ii) to emphasize the effect of partial substitution of Ni with Cu, to enhance SM response; (iii) to analyze the functioning of an actuation setup where an SM and an SE wire are working against each other, and (iv) to introduce a three-fingers gripper with a fast grasping speed, caused by three SMA wires and a slow releasing capacity, due to three super-elastic wires which are directly connected to the SMA ones.

2. Materials and Methods

Here, 0.5 mm-diameter wires were purchased from Kellogg's Research Labs, (New Boston, NH, USA) with three chemical compositions: $Ni_{48}Ti_{52}$; $Ni_{45}Ti_{50}Cu_5$, and $Ni_{48}Ti_{50}Fe_2$. The wires were subjected to: (i) thermal analysis, (ii) WG-SME experiments, (iii) RT tensile testing, (iv) tensile CR-SME investigations, and (v) SM shrinkage biased by SE recovery tests.

Thermal analysis was performed by differential scanning calorimetry (DSC) using a NETZSCH calorimeter type DSC 200 F3 Maya, with a sensitivity below 1 μW, temperature accuracy of 0.1 K, and an enthalpy accuracy below 1%. Calibration was performed with Bi, In, Sn, and Zn standards. Heating scans were performed between RT and 200 °C with a heating rate of 10 °C/min. Calibration curves were also used to exclude any background noise. NiTi, NiTiCu, and NiTiFe wire fragments weighing less than 5 mg were cut and were investigated under an Ar-protective atmosphere. The resulting DSC thermographs, comprising heat flow variations with temperature, were evaluated with the Proteus software v.6.1.

WG-SME experiments were achieved by means of an experimental setup which was recently fully described [40]. Based on the critical temperatures determined on the DSC thermographs, the maximum heating temperatures were selected as 39 °C, 41 °C, 43 °C, and 50 °C. Both NiTi and NiTiCu wires were subjected to WG-SME experiments during which they were elongated by four different loads (2.5, 3, 3.5 and 4 kg) at RT, lifted them during heating and lowered them back during cooling. The entire heating–cooling cycle was controlled by an experimental electronic device specially built for this purpose. The device instantly switched between heating and cooling modes when the maximum pre-set temperature was reached. Experiments were performed with a single heating–cooling cycle for each of the above four maximum temperatures under the effect of each of the four applied loads. In the case of the 4 kg load, five heating–cooling cycles were applied in order to check the reproducibility of the displacement variation with temperature during WG-SME experiments. The results of these experiments consisted of plotting the variations in temperature and the wire's free-end displacement, which were recorded by an acquisition module.

RT tensile tests of NiTi, NiTiCu, and NiTiFe wires were performed on an INSTRON 3382 tensile machine (Norwood, MA, USA). The machine was equipped with a thermal chamber able to heat up to 250 °C. The tests were first performed up to the wire failure and then consisted in loading–unloading up to a maximum strain ranging between 6–8%. Both failure and loading–unloading tests were performed with a cross-head speed of 1 mm/min. To firmly fasten the 0.5 mm-diameter wires, a special type of grips was designed and manufactured. Figure 1 illustrates the details of the experimental grip assemblies which were designed to accommodate a longer wire length, such as to increase the friction force between the wire and grip and to firmly fasten the wire specimen.

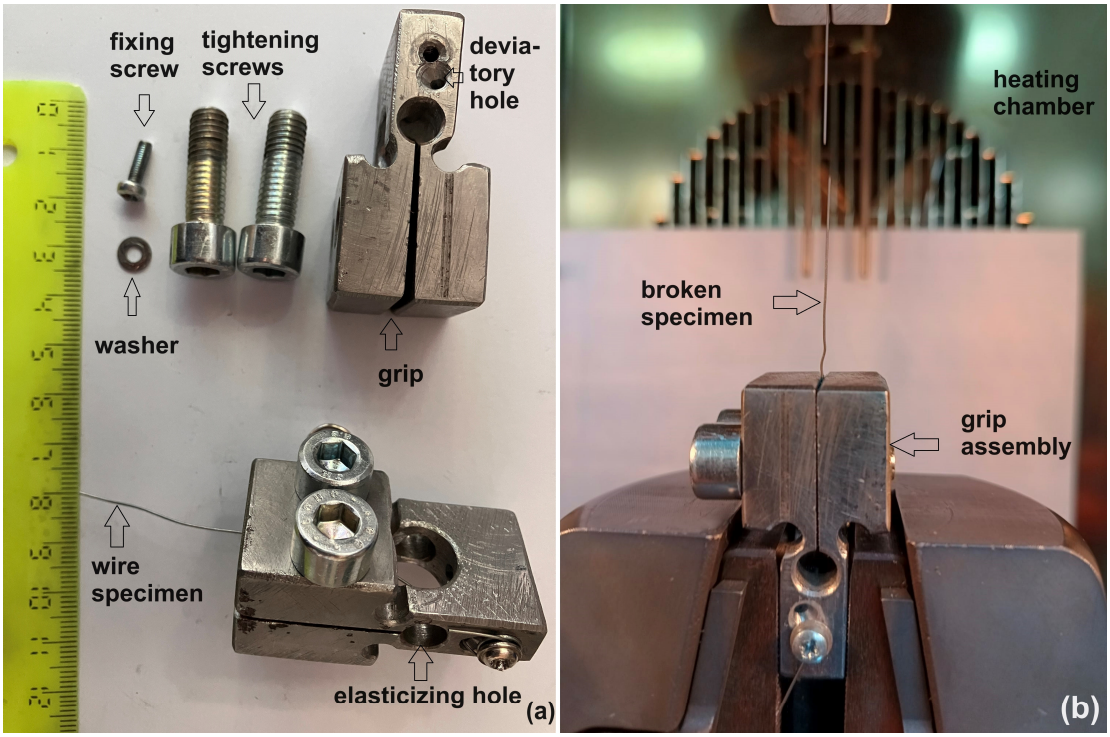

Figure 1. Images of the experimental grip assemblies specially designed for wire testing: (**a**) individual images of the grip assembly in a dissembled state (up) and assembled state with the fixed wire specimen; (**b**) wire specimen failure while being fixed in the lower grip assembly fastened on the tensile testing machine.

The grips were machined from E 335 plain carbon steel. The drilled central elasticizing hole and the final central slot were created using wire spark erosion and enabled the grip body to act as a tweezer, as illustrated in the upper part of Figure 1. The wire specimen passed between the two tightening screws, and then it was tilted through the deviatory hole and wound around the fixing screw. After the final tightening of all three screws, the wire specimen was firmly fastened, as shown in the lower part of Figure 1a. Figure 1b illustrates a wire specimen that failed in tension while being fixed in the lower grip assembly fastened in the thermal chamber of the tensile testing machine.

It must be noted that the SMA wire specimens are rather stiff and hard to bend around the load reduction roller. Moreover, bending alters the structure and induces parasitic mechanical stress on the specimens. To keep the same length for each experiment, the specimens were fastened in the dedicated clamping mechanism by the two large M8 screws. The results of the RT tensile tests comprised stress–strain curves recorded either during tensile failure or during loading–unloading tests. The same grips were used to emphasize CR-SME occurrence.

Tensile CR-SME investigations were performed using the above described tensile testing machine and wire testing grips assemblies. In this case, NiTi and NiTiCu wires were fastened and subjected to two types of investigations. The former comprised emphasizing single CR-SME occurrence, by RT loading–unloading and heating to 56 or 60 °C in an elongated state. The latter consisted of (i) RT loading up to 4% strain, (ii) heating–cooling under 4% constant strain, starting from an elevated stress, (iii) RT additional loading from 4 to 5%, and (iv) heating–cooling under 5% constant strain. The results of these investigations comprised ternary stress–strain–temperature diagrams.

The experiments aiming to monitor the interaction between the SM shrinkage of pre-strained NiTiCu wire and the SE recovery of NiTiFe wire were performed on a special experimental setup designed and fabricated for this study. Figure 2 illustrates the main elements of this setup.

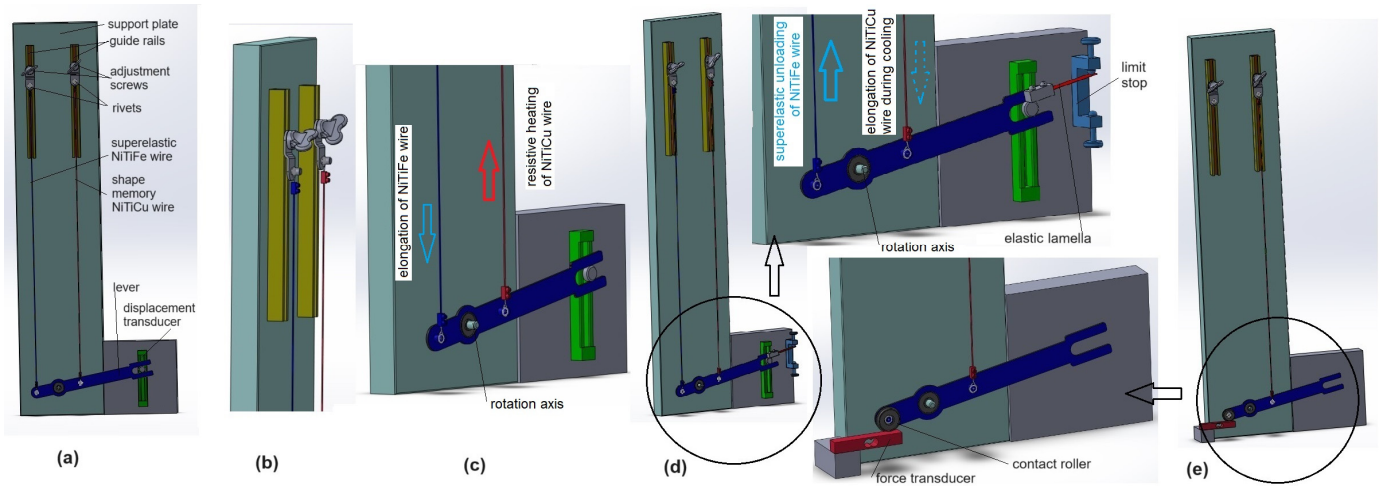

Figure 2. Schematic illustration of the experimental setup for monitoring the interaction between SM shrinkage of NiTiCu wires and SE recovery of NiTiFe wires: (**a**) general view of the experimental setup, displaying the SM (NiTiCu) and the SE (NiTiFe) wires; (**b**) fixing detail of the wire upper ends; (**c**) detail of the lever mechanism with a displacement transducer; (**d**) experimental setup equipped for thermomechanical cycling, with details of the mechanism of stroke reversion; (**e**) experimental setup equipped for force measurement.

Two guide rails are fixed on the support plate. On each rail, one rivet is fixed by means of an adjustment screw. The right-side screw fastens the SM NiTiCu wire specimen, which was pre-strained with approx. 5% force, as it will be pointed out later. The left-side screw fastens the SE NiTiFe wire specimen. The SM-NiTiCu and the SE-NiTiFe wires are fastened in parallel, as shown in Figure 2a. The upper ends of the SM and the SE wires are fixed, as shown in the detail from Figure 2b. The lower ends are connected to a 1st degree leverage, which transmits the displacement from one to the other by rotating around a rotation axis. In addition, the SM NiTiCu wire is coupled to electric connectors at its two ends. When heated, the wire will develop WG-SME and will shrink. The lever will stretch the SE NiTiFe wire, as illustrated in Figure 2c. After cutting off the electric power, the NiTiCu wire will cool down, will become martensitic, and will soften, transmitting less force to the lever, which will allow the SE wire to shrink in order to recover its initial undeformed state. Therefore, in turn, each wire will be elongated by the other, by means of the leverage: the SE NiTiFe wire will be elongated during SM NiTiCu heating which, in turn, will be elongated after becoming softer during cooling as a result of the unloading of the SE NiTiFe wire. Figure 2d illustrates the setup equipped for thermomechanical cycling. The detail shows a flexible elastic lamella fixed at one end of the leverage, which alternatively touches the upper and lower limit stops. During NiTiCu wire heating, it will shrink and rotate the leverage, which will elongate the SE NiTiFe wire, until the flexible elastic lamella touches the upper limit stop, as displayed in Figure 2d. This will stop the electric resistive heating, and the NiTiCu wire will start very quickly to cool down, thus becoming softer. When its stress would become lower than that of the NiTiFe wire, the latter would rotate the leverage clockwise, thus elongating the NiTiCu wire. Thus, the electric resistive heating will be turned on and off, thus determining the oscillating rotation of the leverage. Finally, Figure 2e exemplifies how the force developed by WG-SME of the NiTiCu wire is measured with a force transducer. The results of these experiments have the form of ternary diagrams of the wire's free-end displacement as a function of time and temperature.

3. Results and Discussion

The results of the thermal analysis, WG-SME experiments, RT tensile tests, CR-SME investigations, and SM shrinkage vs. SE recovery experiments are presented and discussed in this section.

3.1. Thermal Analysis

The DSC thermograms recorded during the first heating and second heating–cooling cycle, up to 60 °C, of fragments of the three wires, are illustrated in Figure 3. The first cooling to RT was performed without a controlled temperature variation rate and is missing from the figure.

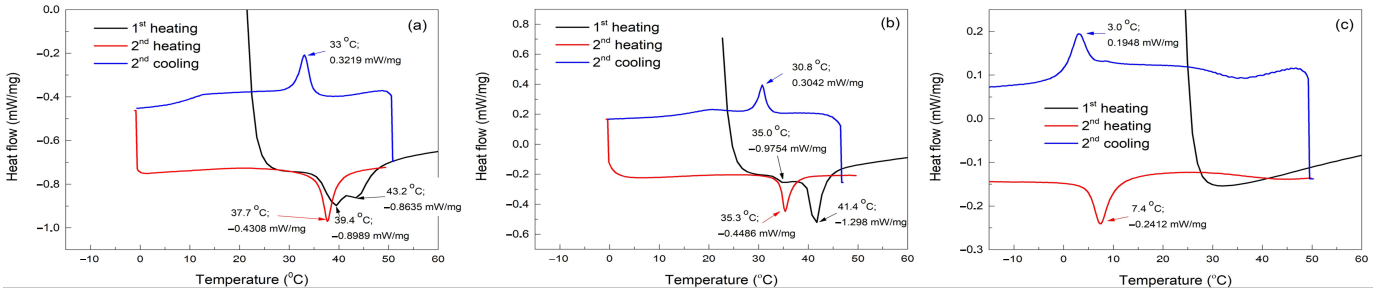

Figure 3. DSC thermograms recorded during the first heating and second heating–cooling cycle to 100 °C of different wire fragments: (**a**) NiTi; (**b**) NiTiCu, and (**c**) NiTiFe.

The presence of an endothermic minimum on the DSC charts recorded during the heating of a martensitic SMA is typically associated with martensite reversion to austenite and represents the mechanism of SME [41].

The martensitic $Ni_{48}Ti_{52}$ SMA wire, which is Ti-rich, would experience, in the first heating, a reverse martensitic transformation, which can be associated with the major endothermic peak located at 39.4 °C, and an R-phase transition [42] located, in this case, at 43.2 °C, according to Figure 3a. During the second heating–cooling cycle, martensite reversion occurred at 37.7 °C because uncontrolled cooling resulted in unstable martensite, which reversed to austenite at lower temperature [17]. When comparing the specific absorbed enthalpies that accompany the two heating-induced transitions, values between 0.86 and 0.9 mW/mg can be observed at the first heating and a value of 0.4308 mW/mg can be observed at the second heating. The second controlled cooling caused martensite formation at 33 °C.

Figure 3b, displaying the heat flow variation during the heating of a fragment of $Ni_{45}Ti_{50}Cu_5$ wire, illustrates two endothermic peaks, during the first heating. The smaller one, located at 35 °C, can be ascribed to the reverse transformation of B19′ monoclinic martensite into B19 orthorhombic martensite [43], while the larger one, located at 41.4 °C corresponds to the reversion of the intermediate B19 martensite [44] to B2 body-centered cubic austenite [45]. From the point of view of the specific absorbed enthalpies, Figure 3b shows that the fragment of $Ni_{45}Ti_{50}Cu_5$ wire required about 0.98 mW/mg for the first transition and 1.3 mW/mg for the second one. During the second heating, martensite reversion occurred in a single step at a lower temperature (35.3 °C), and martensite formation occurred at 30.8 °C.

Finally, Figure 3c displays a thermogram without any transition that corresponds to the super-elastic character of the $Ni_{48}Ti_{50}Fe_2$ wire, which is austenitic at RT [46].

From the above results, it can be concluded that the NiTiCu wire is more suitable for developing WG-SME since it requires a larger amount of specific energy for the reverse martensitic transformation.

3.2. Work-Generating Shape Memory Effect

To compare the WG-SME capacity of the two SM-wires, they were elongated at RT by four loads weighing 2.5, 3, 3.5, and 4 kg, and were resistively heated up to four maximum temperatures selected from the DSC thermograms from Figure 3 as 39 °C, 41 °C, 43 °C, and 50 °C, respectively. The variations in time (which was omitted for simplicity reasons) of the displacement of wire's end where the load is fastened and maximum heating temperature are illustrated in Figure 4 for the TiNi wires and in Figure 5 for the NiTiCu wires.

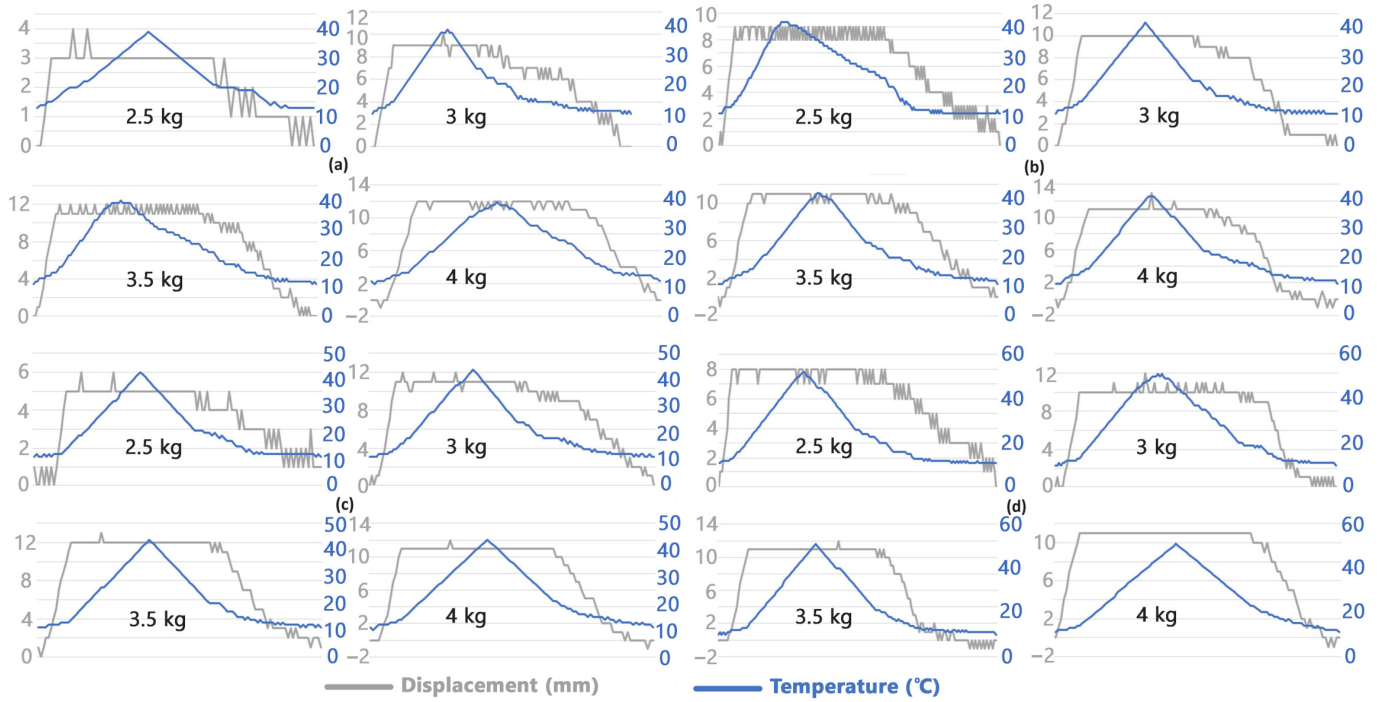

Figure 4. Highlighting the development of WG-SME by NiTi wires, by lifting four loads of 2.5, 3, 3.5 and 4 kg, respectively, during the heating from RT to different temperatures: (**a**) 39 °C; (**b**) 41 °C; (**c**) 43 °C; (**d**) 50 °C.

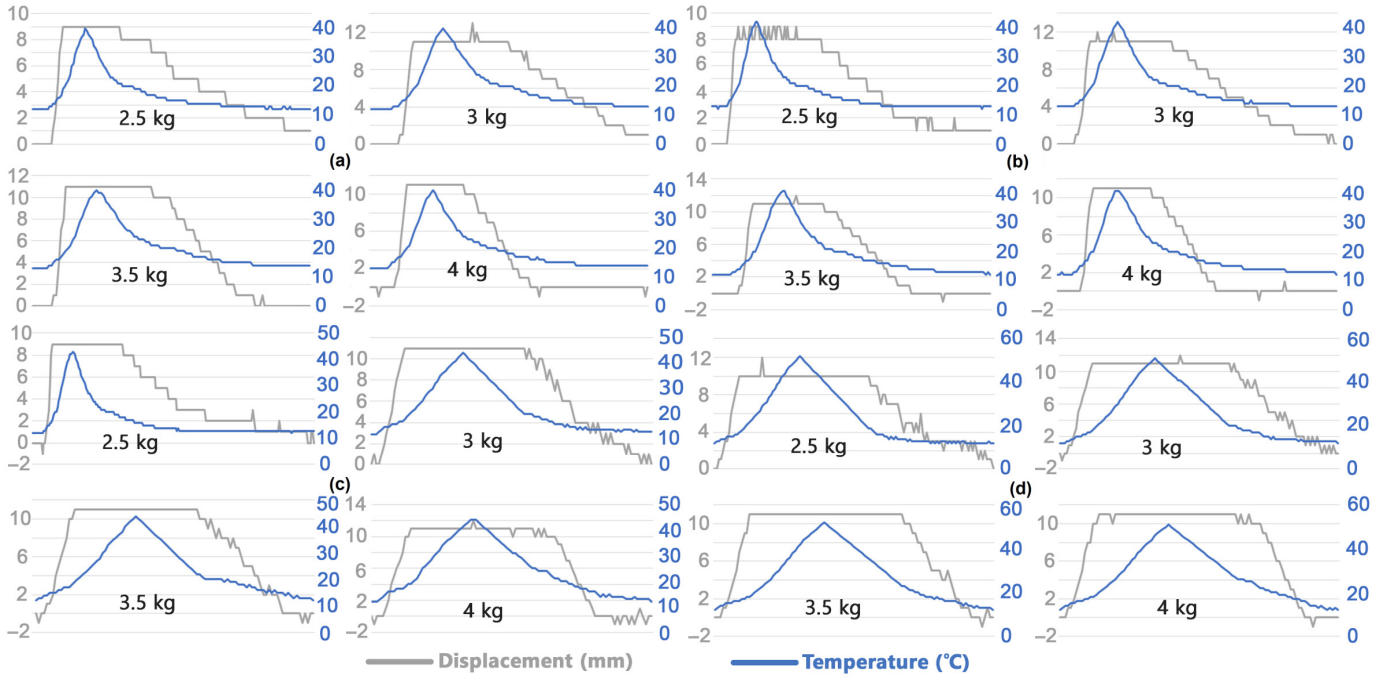

Figure 5. Highlighting the development of WG-SME by NiTiCu wires, by lifting four loads of 2.5, 3, 3.5 and 4 kg, respectively, during the heating from RT to different temperatures: (**a**) 39 °C; (**b**) 41 °C; (**c**) 43 °C; (**d**) 50 °C.

In all of the 16 diagrams from Figure 4, the wires that were elongated at RT by the applied loads shrunk during heating and lifted the loads. The smaller loads, such as 2.5 and 3 kg, could not elongate the wire to a greater extent at RT. For this reason, the displacements

associated with these loads were lower. Conversely, the highest displacements were associated with the higher loads, namely 3.5 and 4 kg.

The maximum vertical displacement was 12 mm = 0.012 m and the maximum load lifted along this distance was 4 kg, as in Figure 4a. It follows that the maximum work, developed by the NiTi wire was 0.012 m $\times$ 9.8 ms^{-2} $\times$ 4 kg $\approx$ 0.47 J.

Another noticeable fact is the delay between the variations of displacement and temperature. The former varies much faster, reaches the maximum value, and remains constant, while the latter is still varying. This is due to the thermal inertia of the temperature-measuring thermistor.

Figure 5 displays the variations of the displacement of the $Ni_{45}Ti_{50}Cu_5$ wire end with ah attached load and the maximum electric resistive heating temperature.

When comparing Figures 4 and 5, two features can be noticed, as follows:

- NiTiCu wires warmed up faster than the NiTi ones;
- The displacements developed by the NiTiCu wires were slightly lower than those developed by the NiTi wires, compared to which they were smoother and had shorter maintaining times.

Aiming to compare the cycling capacities of the two SM wires, during repetitive WG-SME development, they were subjected to five cycles of resistive heating up to a maximum temperature of 50 °C, with an applied load of 4 kg. The results are illustrated in Figure 6.

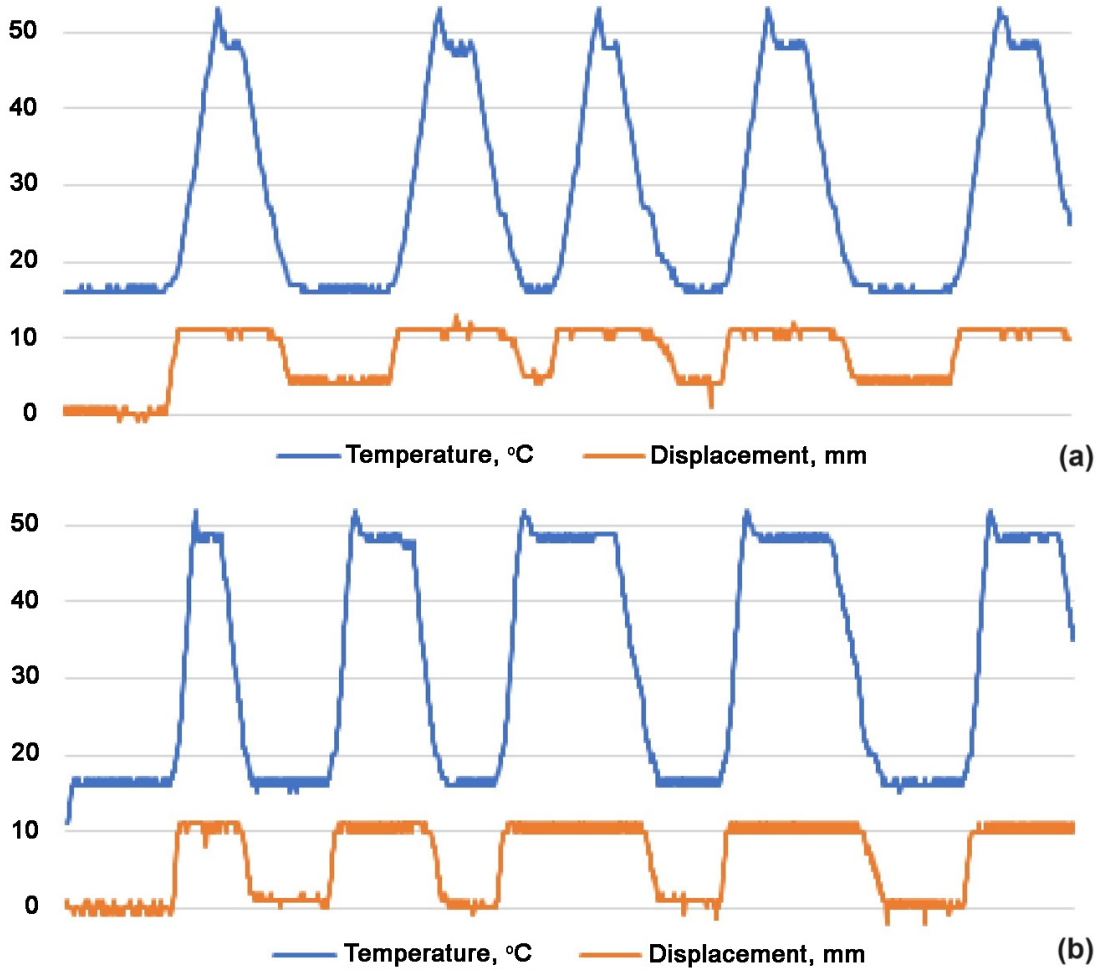

Figure 6. Highlighting the development of repetitive WG-SME during the repetitive heating from RT to 50 °C, with a hanging load of 4 kg: (**a**) NiTi; (**b**) NiTiCu.

Figure 6 shows that there are the following differences between the repetitive development of WG-SME by the two SM wires:

- From the point of view of temperature variation, the NiTiCu wire warmed up faster, cooled down faster and maintained the maximum temperature longer than the NiTi wire, though the two wires had the same diameter and length;
- From the point of view of displacement variation, it is obvious that the NiTiCu wire developed a larger stroke, about 10 mm, while the NiTi wire remained elongated after the first heating–cooling cycle.

These results demonstrate that both SM wires were able to develop repetitive WG-SME, but the NiTiCu wire was able to develop a larger stroke and a maximum work of 0.392 J.

3.3. Tensile Behavior at Room Temperature

The tensile failure curves at RT of the three wires are illustrated in Figure 7

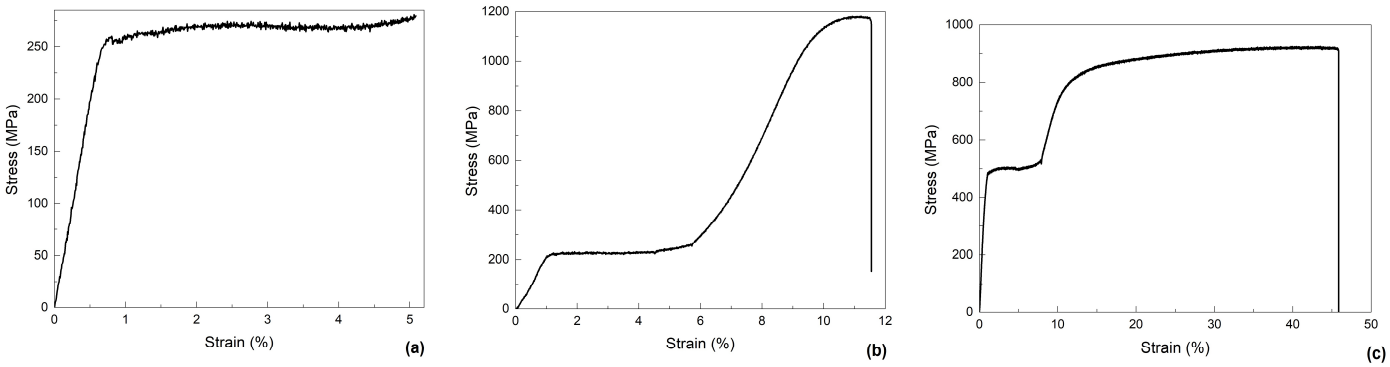

Figure 7. Tensile failure curves at RT of different wire specimens: (**a**) NiTi; (**b**) NiTiCu; (**c**) NiTiFe.

The main mechanical parameters, (E—Young's modulus; $R_{y,m}$—yield and failure strength, and $\varepsilon_{y,m}$—yield and failure strains) of the three failure curves are summarized in Table 1.

Table 1. Mechanical parameters of the tensile failure curves from Figure 7.

Wire Material	E	R_y	R_m	ε_y	ε_m
	GPa	MPa	MPa	%	%
$Ni_{48}Ti_{52}$;	38	259	279	0.8	5
$Ni_{45}Ti_{50}Cu_5$	23	220	1177	1.2–5.7	12
$Ni_{48}Ti_{50}Fe_2$	56	481	925	1-7.7	46

These results confirm the beneficial effects of ternary alloying of NiTi SMAs, if one considers that both the NiTiCu and NiTiFe wires exhibit larger values of failure stress and strain.

The next tensile tests were performed by loading–unloading, with the aim of monitoring the mechanical response of NiTi-based wires when subjected to reversible deformation. The resulting tensile loading–unloading curves are illustrated in Figure 8, for the three alloy wires under study.

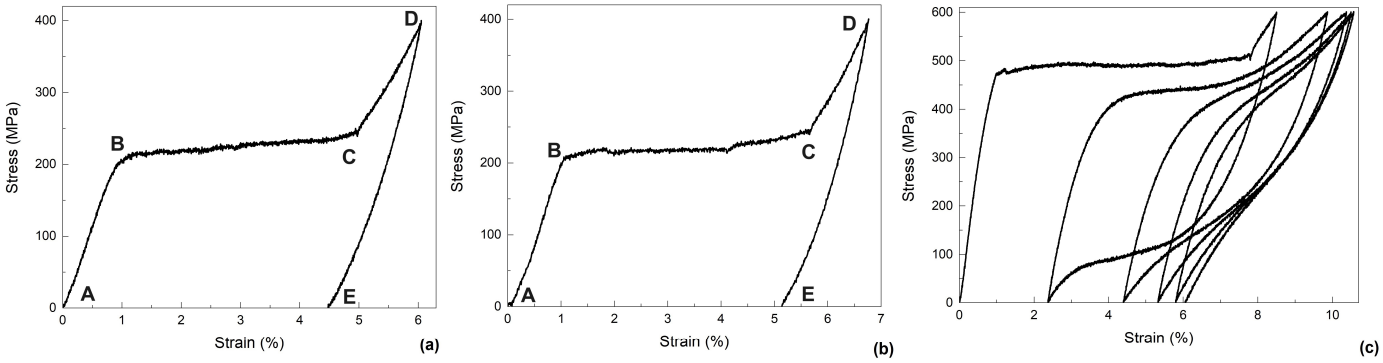

Figure 8. Tensile loading–unloading curves at RT of different wire specimens: (**a**) NiTi; (**b**) NiTiCu; (**c**) NiTiFe (please see text for explanations).

The two diagrams from Figure 8a,b are typical for the plastic deformation of the SMAs that experience a thermoelastic martensitic transformation [47]. The first quasi-linear portion (AB) corresponds to the elastic deformation of the martensitic wires (as shown in Figure 3, both $Ni_{48}Ti_{52}$ and $Ni_{45}Ti_{50}Cu_5$ wires were martensitic at RT). The stress plateaus (BC) are generally associated with the crystallographic reorientation of martensite by detwinning. Further deformation caused the elastic deformation of detwinned martensite (CD) which springs back during unloading (DE) [48]. On the other hand, the diagrams from Figure 8c, revealing an unloading stress plateau, are typical for the super-elastic response of the $Ni_{48}Ti_{50}Fe_2$ SMA wires [49]. When increasing the number of cycles, both the loading and unloading stress plateaus became shorter and more inclined, while permanent strain increased in terms of absolute value but relatively decreased at the cycle level [50]. For this reason, the SE description was reduced from an unloading stress plateau to an unloading inflection point.

3.4. Constrained Recovery Shape Memory Effect

The typical curves, displaying stress variation during RT loading–unloading followed by constant strain-heating, are illustrated in Figure 9, for the NiTi and NiTiCu wires.

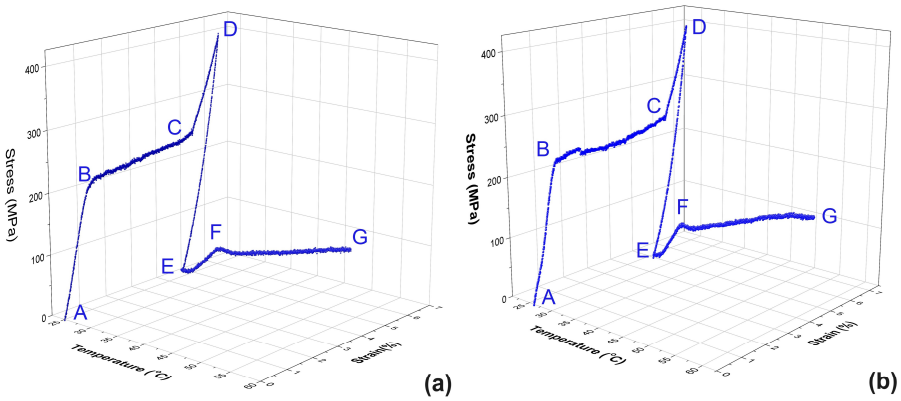

Figure 9. Emphasizing CR-SME after RT tensile loading–unloading and heating at a constant strain: (**a**) NiTi heated to 56 °C; (**b**) NiTiCu heated to 60 °C (please see text for explanations).

The characteristic stages of the RT loading–unloading can be easily identified along the A–B–C–D–E route, which coincides with the points designated in Figure 8. In point E, approximate values of 4.5% and 5% were obtained for the permanent strain in Figure 9a and in Figure 9b, respectively.

The crosshead of the tensile testing machine was blocked, so the respective permanent strains were subsequently kept constant and the heating chamber was turned on. During heating, stress increased abruptly up to point F which corresponds to the first endothermic

peak of the DSC thermograms from Figure 3a,b and represents the midpoint of the reverse martensitic transformation.

To explain this initial stress increase, one must consider that, during the first half of the reverse martensitic transition, the transformation rate increases and stabilizes. Then, in the second half, it remains constant upon further heating, and then it finally decreases [51].

The transformation rate increase, between E and F, could be the cause of the abrupt stress rise at the beginning of heating, when SME-induced strain recovery counteracts thermal expansion. The former causes a stress rise, since it tends to stretch the wire specimen, while the latter tends to increase the wire's length, thus reducing the tensile stress.

The continuation of the heating process initially caused an initial stress decrease with several MPa, then a slow continuous gradual increase up to 123 MPa for the NiTi wire and 147 MPa for NiTiCu.

The initial stress decrease can be associated with the transformation rate diminution in the second half of the reverse martensitic transformation in such a way that thermal expansion becomes the most prominent phenomenon. At higher temperatures, R-phase/B19 martensite reversion to B2 austenite is completed in such a way that SME-induced shrinkage again becomes the prominent phenomenon and the tensile stress rises because B2 austenite has a smaller relative volume than both R-phase and B19 martensite [52].

Aiming to determine the behavior of the two SM-wires when undergoing repetitive CR-SME tests, according to the mechanical response from Figure 10, the specimens were (i) elongated to 4% strain at RT, 0–1 and kept in a stressed state in point 1, (ii) heated under a constant strain up to 56 or 60 °C, 1–2, (iii) cooled to RT under constant strain, 2–3, and additionally loaded from 4 to 5%, 3–4, for a second cycle of CR heating (4–5) and cooling (5–6), according to the same routine as in the first cycle.

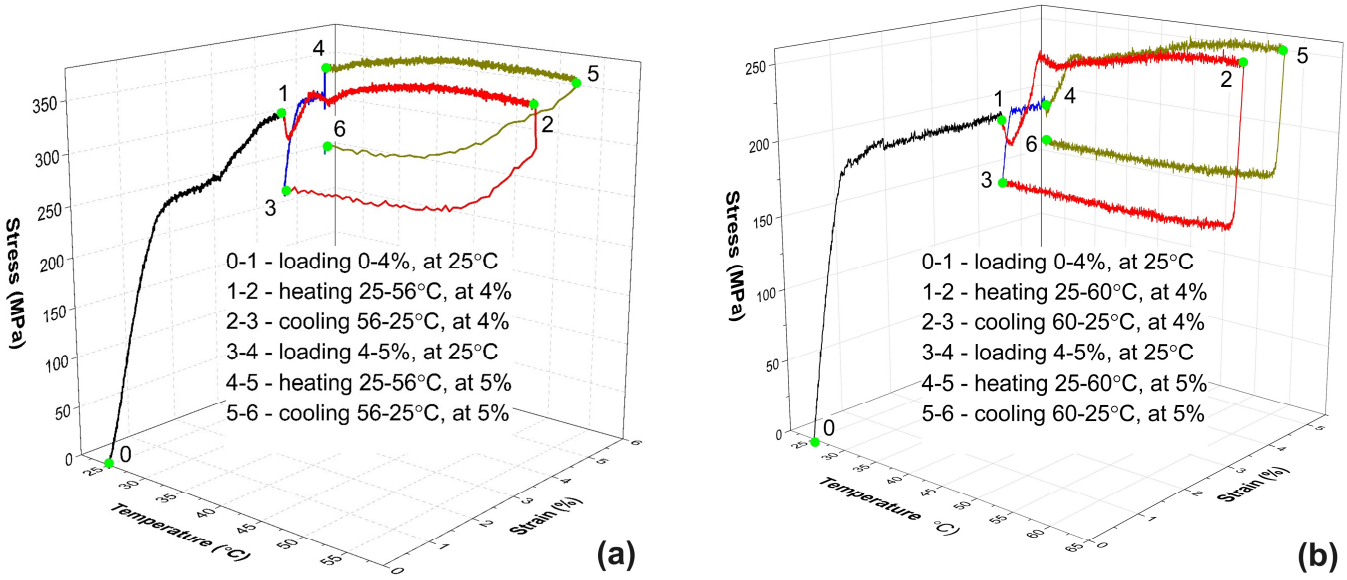

Figure 10. Emphasizing CR-SME during two cycles comprising 0–1 = RT tensile loading to 4%, 1–2 = heating at constant strain, 2–3 = cooling at constant strain, 3–4 = RT loading from 4 to 5%, 4–5 = heating at constant strain, 5–6 = cooling at constant strain: (**a**) NiTi heated up to 56 °C; (**b**) NiTiCu heated up to 60 °C.

It is obvious that even when the two wire specimens were heated up to the same maximum temperatures as in Figure 9, the stress increase was smaller in Figure 10. Thus, for the NiTi wire, stress increased by 123 MPa, when starting from 0, and with approx. 50 MPa after additional loading between two heating–cooling cycles, when starting from 300 MPa. On the other hand, the corresponding rise was 147 MPa and with approx. 70 MPa, when starting from 180 MPa, respectively.

As such, the following can be concluded:

- The NiTiCu wire experienced a larger relaxation capacity during cooling, in good accordance with the WG-SME response from Figure 6;
- Both SM-wires were able to develop repetitive CR-SME.

3.5. Actuation System Based on SM Shrinkage vs. SE Recovery

The final set of tests was performed on the experimental setup and monitored the evolution of the NiTiCu SM-wire working against that of the SE NiTiFe wire. The results are summarized in Figure 11.

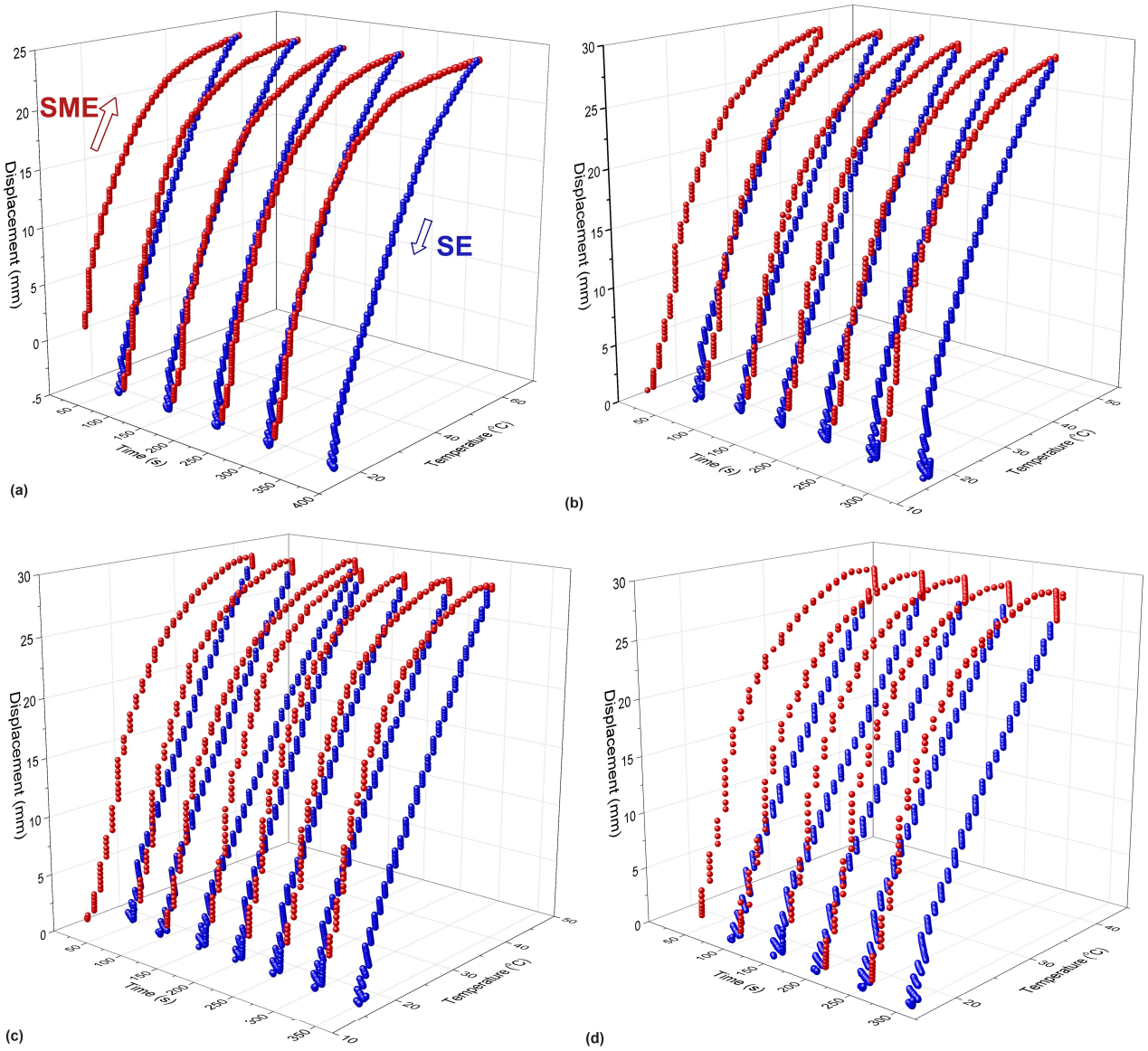

Figure 11. Emphasizing the variation in the shrinkage of the $Ni_{45}Ti_{50}Cu_5$ SM wire biased by the unloading recovery of the SE $Ni_{48}Ti_{50}Fe_2$ wire, at different maximum voltage values of the electric current used for resistive heating: (**a**) 3.5 V; (**b**) 4 V; (**c**) 4.5 V; (**d**) 5 V.

The martensitic NiTiCu wire was pre-strained at RT with 5%. For actuation, four voltages were used, as pointed out in Figure 11. During resistive heating, SME occurred and stretched the NiTiCu wire which, in turn, elongated the SE NiTiFe wire by means of the leverage, as specified in Figure 2. When the elastic lamella shown in Figure 2d touched the upper limit stop, resistive heating was interrupted and the NiTiCu wire started to cool

down. During the transformation of austenite into martensite, the NiTiCu wire softened and gradually became elongated by the NiTiFe wire. As can be observed from Figure 11 and from the Supplementary Material Video S1, the displacement rate was much larger during SME development than during super-elastic recovery. Actually, SM shrinkage occurred in a few seconds while SE recovery took about 50 s. Nevertheless, the process has been reproducible for several tens of cycles. For example, Figure S1 from the Supplementary Materials displays cycles recorded during a 40 min period. Displacement variation was recorded every five cycles, with SME being caused by a 4 V voltage-heating effect. It can be noticed that the displacement loops tend to become narrower with the increase in the number of cycles. This could be a training effect that is frequently observed in NiTiCu SMAs, as it was previously reported by some of the present authors [53].

From an energetic point of view, the setup consumed energy during SME development when loading the NiTiFe wire and restored it during super-elastic unloading. So, the area under the loading curve (corresponding to displacement variation during SME development) is proportional to the amount of consumed energy, W_0, while the area under the unloading curve (corresponding to super-elastic recovery) is proportional to the amount of restored energy, W_{rec}. These area values are summarized in Table 2.

Table 2. Variation in the surface areas proportional to specific consumed (W_o) and restored (W_{rec}) energies during SM vs. SE displacement cycles (a.u.).

	1st Cycle		2nd Cycle		3rd Cycle		4th Cycle		5th Cycle	
	W_0	W_{rec}	W_0	W_{rec}	W_0	W_{rec}	W_0	W_{rec}	W_0	W_{rec}
3.5 V	640.35	393.55	687.2	452.5	644.7	455.6	663.35	455.8	762.85	504.7
4 V	630.9	418.3	680.45	458.2	664.75	465.35	644.8	443.6	637.65	468.95
4.5 V	550.45	341.55	550.5	356.2	666.8	429.8	529.7	338.85	549.6	362.8
5 V	281.7	240.5	460	260.6	506.15	282.3	502.95	291.95	509.45	302.8

By subtracting the restored energy from the consumed energy and dividing the result ($\Delta W = W_0 - W_{rec}$) by the consumed energy one, can calculate the specific energy dissipated by internal friction, as shown in Figure 12.

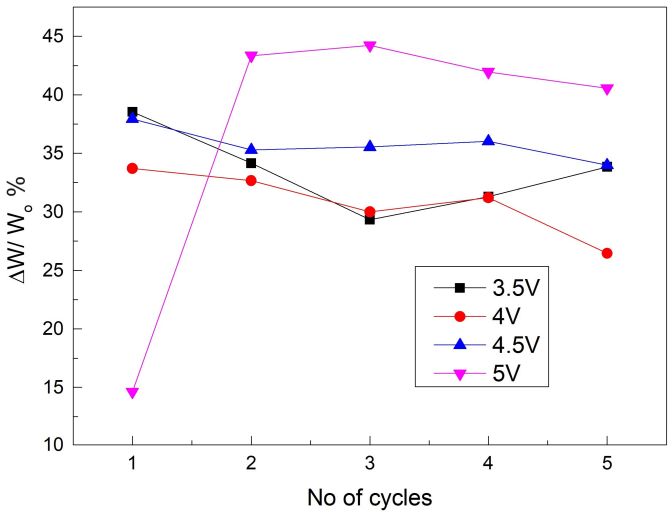

Figure 12. Variations in the specific energy, dissipated by internal friction, during consecutive cycles of resistive heating-induced SM shrinkage of the $Ni_{45}Ti_{50}Cu_5$ SM wire compensated by unloading recovery of the $Ni_{48}Ti_{50}Fe_2$ SE wire.

Figure 12 confirms the decreasing tendency of the thermal hysteresis, proportional to the area between the loading and unloading curves [54], with the increase in the number of cycles.

Based on the above observations, a robotic gripper was designed. The device was built up by adapting a NiTiCu and a NiTiFe wire, as an actuating element, on a classical gripper, as illustrated in Figure 13.

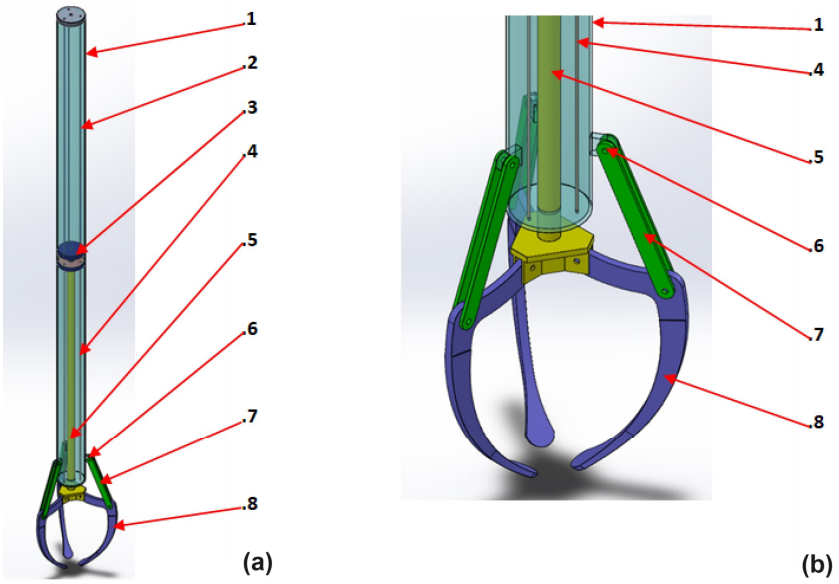

Figure 13. Design of a robotic gripper, actuated with a NiTiCu SM and NiTiFe SE wires: 1—housing; 2—NiTiFe wires; 3—piston; 4—NiTiCu wires; 5—fork; 6—pins; 7—connecting rods; 8—claws. (**a**) general view; (**b**) detail of the grasping system.

The system comprises a housing (1), three NiTiFe SE wires (2), a piston (3), three NiTiCu SM wires (4), a fork (5), nine pins (6), six connecting rods (7), and three claws (8) that act as gripping elements. The NiTiCu wires (4) are in the martensitic state at room temperature, being pre-strained and connected with one end at the housing base and with the other end to the piston, as illustrated in Figure 13b. The NiTiFe wires (2) are connected with one end at the piston and with the other end to the top of the housing. Their role is to act as a bias element. Thus, while being non-actuated, the NiTiCu wires are softer than the NiTiFe wires, being pre-strained and fixed in the assembly in an elongated martensitic state.

During resistive heating, by means of the electric connection wires shown in Figure 14a, the NiTiCu wires stretch back, since they become tougher than the NiTiFe wires, thus causing the translation of the piston (3) which moves the fork (5). After cutting the power, the NiTiCu wires start to cool, regain the martensitic state, and became softer than the NiTiFe wires, which move the piston back in the initial position.

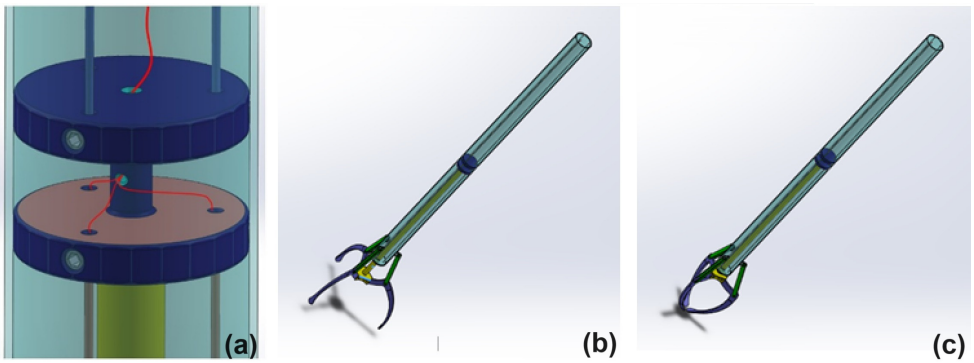

Figure 14. Details of the gripping device: (**a**) electric connection wires; (**b**) open position; (**c**) closed position.

The claws (8) are articulated at one end to the fork and at the middle to the housing, by means of the connecting rods (7). The piston translation causes a rotation movement of the claws, hence the device being able to grip and release loads, as illustrated in Figure 14b,c, respectively. The robotic gripper is able to grab various objects, with the action controlled by electric resistive heating of the NiTiCu wire, and to release them in a fixed position, with the action controlled by the super-electic recovery of the elongated NiTiFe wire.

4. Summary and Conclusions

By summarizing the above results, the following conclusions may be drawn.

1. From the point of view of WG-SME:
   - The SM response (RT displacement) increased with the applied load up to 12 mm, corresponding to a work of 0.47 J;
   - Cu addition caused higher heating and cooling rates during single tests and larger displacement during cyclic tests, developing a repetitive work of 0.392 J.
2. From the point of view of the RT tensile behavior:
   - Both $Ni_{48}Ti_{52}$ and $Ni_{45}Ti_{50}Cu_5$ wires exhibited stress plateaus during loading associated with the crystallographic reorientation of martensite;
   - The $Ni_{48}Ti_{50}Fe_2$ wire had stress plateaus both during loading and unloading, associated with a reversible stress induced martensitic transformation, which changed to inflection points during cycling.
3. From the point of view of CR-SME:
   - $Ni_{48}Ti_{52}$ and $Ni_{45}Ti_{50}Cu_5$ wires elongated with 4.5 and 5% developed CR stresses of 123 MPa and 147 MPa, when heated to 56 and 60 °C, respectively;
   - Both $Ni_{48}Ti_{52}$ and $Ni_{45}Ti_{50}Cu_5$ wires, when heated in elongated state, developed repetitive stress–temperature variations;
   - Cu addition caused a larger relaxation capacity during cooling.
4. From the point of view of the trade-off between SM shrinkage and SE recovery:
   - When heated under the effect of a voltage of 4.5–5 V, the 5% pre-strained $Ni_{45}Ti_{50}Cu_5$ wires developed a 28 mm stroke which elongated the $Ni_{48}Ti_{50}Fe_2$ wire by means of leverage;
   - When air-cooled, the $Ni_{45}Ti_{50}Cu_5$ wires were elongated again by the unloading recovery of the $Ni_{48}Ti_{50}Fe_2$ wire;
   - SM shrinkage lasted a few seconds, while and SE recovery lasted up to 50 s;
   - SM vs. SE displacement cycles could be repeated for tens of cycles, during which time a decreasing tendency of the specific energy dissipated by internal friction was noted;
   - A robotic gripper was designed based on the antagonistic deformation of $Ni_{45}Ti_{50}Cu_5$ and $Ni_{48}Ti_{50}Fe_2$ wires;
   - Compared to classical solutions, with hydraulic or mechanical actuation, the proposed system is more compact, rapid, economical, and ergonomic. Compared to other SMA-driven systems, the present solution can provide the manipulated objects' fast grasping and slow release speeds.
   - General conclusions:
   - Here, 0.5 mm-diameter martensitic $Ni_{48}Ti_{52}$ and $Ni_{45}Ti_{50}Cu_5$ wires were able to perform both WG-SME and CR-SME by repetitively lifting loads up to 4 kg, (developing works of 0.392–0.47 J) and by generating stress of 123–147 MPa (when pre-strained with 4.5 and 5%), respectively;
   - Here, 5% pre-strained martensitic $Ni_{45}Ti_{50}Cu_5$ wires and austenitic $Ni_{48}Ti_{50}Fe_2$ wires developed a 28 mm stroke by SM/SE coupling, which was repeated during tens of cycles and accompanied by a decreasing tendency of energy dissipation by internal friction.

- The simulated three-fingers gripper has the potential to develop rapid grasping forces and slow release rates due to the direct coupling of pre-strained SM and SE wires.
- After manufacturing the gripper, additional experiments have to be performed to determine its real grasping and releasing rates and to test the training effect on these rates.

Supplementary Materials: The following supporting information can be downloaded at: https://www.mdpi.com/article/10.3390/act13080319/s1, Video S1: SM vs. SE 2 cycles; Figure S1: SM vs. SE displacement cycles recorded during a 40 min period.

Author Contributions: Conceptualization, L.-G.B.; methodology, B.P.; software, A.P.T., B.P. and R.I.C.; validation, B.P.; formal analysis, N.-M.L. and M.P.; investigation, A.P.T., N.-M.L. and R.I.C.; resources, L.-G.B. and M.P.; data curation, R.I.C.; writing—original draft preparation, L.-G.B.; writing—review and editing, M.P. and I.D.; visualization I.D.; supervision, N.-M.L.; project administration, A.P.T. and L.-G.B.; funding acquisition, I.D. All authors have read and agreed to the published version of the manuscript.

Funding: This research received no external funding.

Data Availability Statement: The original contributions presented in the study are included in the article/Supplementary Material, further inquiries can be directed to the corresponding author.

Conflicts of Interest: The authors declare no conflicts of interest.

References

1. Wayman, C.M. Deformation, Mechanisms and Other Characteristics of Shape Memory Alloys. In *Shape Memory Effects in Alloys*; Perkins, J., Ed.; Plenum Press: New York, NY, USA, 1975; pp. 1–27.
2. Otsuka, K.; Wayman, C.M. (Eds.) Introduction. In *Shape Memory Materials*; Cambridge University Press: Cambridge, UK, 1998; pp. 1–26.
3. Lohan, C.; Pricop, B.; Comaneci, R.I.; Cimpoesu, N.; Bujoreanu, L.G. Variation tendencies of tensile constrained recovery behaviour and associated structural changes during thermal cycling of a Fe-Mn-Si-Cr-Ni shape memory alloy. *Optoelectron. Adv. Mater.* **2010**, *4*, 816–820.
4. Lieberman, D.S.; Schmerling, M.A.; Carz, R.W. Ferroelastic "Memory" and Mechanical Properties in AuCd. In *Shape Memory Effects in Alloys*; Perkins, J., Ed.; Plenum Press: New York, NY, USA, 1975; pp. 203–244.
5. Buehler, W.J.; Gilfrich, J.V.; Wiley, R.C. Effect of Low-Temperature Phase Changes on the Mechanical Properties of Alloys near Composition TiNi. *J. Appl. Phys.* **1963**, *34*, 1475–1477.
6. Ohkata, I.; Suzuki, Y. The design of shape memory alloy actuators and their applications. In *Shape Memory Materials*; Otsuka, K., Wayman, C.M., Eds.; Cambridge University Press: Cambridge, UK, 1998; pp. 240–266.
7. Nayan, N.; Singh, G.; Murty, S.V.S.N.; Narayana, P.R.; Mohan, M.; Venkitakrishnan, P.V.; Ramamurty, U. Effect of ternary additions of Cu and Fe on the hot deformation behavior of NiTi shape memory alloy—A study using processing maps. *Intermetallics* **2021**, *131*, 107084. [CrossRef]
8. Velmurugan, C.; Senthilkumar, V. The effect of Cu addition on the morphological, structural and mechanical characteristics of nanocrystalline NiTi shape memory alloys. *J. Alloys Compd.* **2018**, *767*, 944–954. [CrossRef]
9. Liu, X.; Li, H.; Zhang, Y.; Yang, Z.; Gu, Q.; Wang, X.; Zhang, Y.; Yang, J. Cryogenic temperature deformation behavior and shape memory mechanism of NiTiFe alloy. *Intermetallics* **2023**, *162*, 107997. [CrossRef]
10. Lotkov, A.; Grishkov, V.; Timkin, V.; Baturin, A.; Zhapova, D. Yield stress in titanium nickelide-based alloys with thermoelastic martensitic transformations. *Mater. Sci. Eng. A* **2019**, *744*, 74–78. [CrossRef]
11. Oliveira, J.P.; Zeng, Z.; Berveiller, S.; Bouscaud, D.; Fernandes, F.B.; Miranda, R.M.; Zhou, N. Laser Welding of Cu-Al-Be Shape Memory Alloys: Microstructure and Mechanical Properties. *Mater. Design* **2018**, *148*, 145–152. [CrossRef]
12. Mohan, S.; Banerjee, A. Particle filter based self sensing Shape Memory Alloy wire actuator under external cooling. *Mech. Syst. Signal Proc.* **2023**, *185*, 109779. [CrossRef]
13. Rao, Z.; Wang, X.; Leng, J.; Yan, Z.; Yan, X. Design methodology of the $Ni_{50}Ti_{50}$ shape memory alloy beam actuator: Heat treatment, training and numerical simulation. *Mater. Design* **2022**, *217*, 110615. [CrossRef]
14. Holschuh, B.; Obropta, E.; Newman, D. Low Spring Index NiTi Coil Actuators for Use in Active Compression Garments. *IEEE/ASME Trans. Mechatron.* **2015**, *20*, 1264–1277. [CrossRef]
15. Wang, J.; Huang, B.; Gu, X.; Zhu, J.; Zhang, W. Actuation performance of machined helical springs from NiTi shape memory alloy. *Int. J. Mech. Sci.* **2022**, *236*, 107744. [CrossRef]
16. Lu, Y.; Jiang, J.; Zhang, J.; Zhang, R.; Zhang, Q.; Zhou, Y.; Wang, L.; Yue, H. A dynamic stiffness improvement method for thin plate structures with laminated/embedded shape memory alloy actuators. *Thin Walled Struct.* **2022**, *175*, 109286. [CrossRef]

17. Jani, J.M.; Leary, M.; Subic, A.; Gibson, M.A. A review of shape memory alloy research, applications and opportunities. *Mater. Design* **2014**, *56*, 1078–1113. [CrossRef]
18. Yurtsever, O.; Küçük, H. Design, production and vision based analysis of a wireless operated 2-DOF SMA driven soft robotic arm. *Mater. Mater. Today Commun.* **2023**, *34*, 105176. [CrossRef]
19. Lu, Y.; Xie, Z.; Wang, J.; Yue, H.; Wu, M.; Liu, Y. A novel design of a parallel gripper actuated by a large-stroke shape memory alloy actuator. *Int. J. Mech. Sci.* **2019**, *159*, 74–80. [CrossRef]
20. Amadi, A.; Mohyaldinn, M.; Ridha, S.; Ola, V. Advancing engineering frontiers with NiTi shape memory alloys: A multifaceted review of properties, fabrication, and application potentials. *J. Alloys Compd.* **2024**, *976*, 173227. [CrossRef]
21. Nicholson, D.E.; Benafan, O.; Bigelow, G.S.; Pick, G.; Demblon, A.; Mabe, J.H.; Karaman, I.; Van Doren, B.; Forbes, D.; Sczerzenie, F.; et al. Standardization of Shape Memory Alloys from Material to Actuator. *Shape Mem. Superelasticity* **2023**, *9*, 353–363. [CrossRef]
22. Nespoli, A.; Besseghini, S.; Pittaccio, S.; Villa, E.; Viscuso, S. The high potential of shape memory alloys in developing miniature mechanical devices: A review on shape memory alloy mini-actuators. *Sens. Actuators A* **2010**, *158*, 149–160. [CrossRef]
23. Baek, H.; Khan, A.M.; Kim, Y. A bidirectional rotating actuator by using a single shape memory alloy wire in a double bend shape. *Sens. Actuators A* **2023**, *360*, 114526. [CrossRef]
24. Kennedy, S.; Shougat, M.R.E.U.; Perkins, E. Robust self-sensing shape memory alloy actuator using a machine learning approach. *Sens. Actuators A* **2023**, *354*, 114255. [CrossRef]
25. Hamid, Q.Y.; Wan Hasan, W.Z.; Azmah Hanim, M.A.; Nuraini, A.A.; Hamidon, M.N.; Ramli, H.R. Shape memory alloys actuated upper limb devices: A review. *Sens. Actuators Rep.* **2023**, *5*, 100160. [CrossRef]
26. Shukla, S.; Barjibhe, R. An experimental and numerical comparison of traditional spring DVA in parallel and shape memory alloy actuated DVA in series and parallel for fixed beam vibration control. *Mater. Today Proc.* **2023**. [CrossRef]
27. Schuleit, M.; Becher, M.; Franke, F.; Maaß, B.; Esen, C. Development of form-fit connection for NiTi shape memory wire actuators using laser processing. *Procedia CIRP* **2020**, *94*, 546–550. [CrossRef]
28. Sgambitterra, E.; Greco, C.; Rodino, S.; Niccoli, F.; Furgiuele, F.; Maletta, C. Fully coupled electric-thermo-mechanical model for predicting the response of a SMA wire activated by electrical input. *Sens. Actuators A* **2023**, *362*, 114643. [CrossRef]
29. Liu, Y.N.; Liu, Y.; Van Humbeek, J. Two-way shape memory effect developed by martensite deformation in NiTi. *Acta Mater.* **1998**, *47*, 199–209. [CrossRef]
30. Liu, R.; Zhang, C.; Ji, H.; Zhang, C.; Qiu, J. Training, Control and Application of SMA-Based Actuators with Two-Way Shape Memory Effect. *Actuators* **2023**, *12*, 25. [CrossRef]
31. Eggeler, G.; Hornbogen, E.; Yawny, A.; Heckmann, A.; Wagner, M. Structural and functional fatigue of NiTi shape memory alloys. *Mater. Sci. Eng. A* **2004**, *378*, 24–33. [CrossRef]
32. Mizzi, L.; Hoseini, S.F.; Formighieri, M.; Spaggiari, A. Development and prototyping of SMA-metamaterial biaxial composite actuators. *Smart Mater. Struct.* **2023**, *32*, 035027. [CrossRef]
33. Ben Zohra, M.; Er-Remyly, O.; Riad, A.; Alhamany, A. Finite element analysis for fatigue phenomena in mechatronic shape memory alloy actuator. *Sci. Afr.* **2023**, *20*, e01601. [CrossRef]
34. Liu, Q.; Ghodrat, S.; Jansen, K.M.B. Design and modelling of a reversible shape memory alloy torsion hinge actuator. *Mater. Design* **2024**, *237*, 112590. [CrossRef]
35. O'Toole, K.T.; McGrath, M.M.; Coyle, E. Analysis and Evaluation of the Dynamic Performance of SMA Actuators for Prosthetic Hand Design. *J. Mater. Eng. Perform.* **2009**, *18*, 781–786. [CrossRef]
36. Dinakaran, V.P.; Balasubramaniyan, M.P.; Muthusamy, S.; Panchal, H. Performa of SCARA based intelligent 3 axis robotic soft gripper for enhanced material handling. *Adv. Eng. Softw.* **2023**, *176*, 103366. [CrossRef]
37. Yang, C.; Wu, X.; Zhu, Y.; Wu, W.; Tu, Z.; Zhou, J. Recent Progress of an Underwater Robotic Avatar. In *Intelligent Robotics and Applications*; Yang, H., Liu, H., Jun, Z., Yin, Z., Liu, L., Yang, G., Ouyang, X., Wang, Z., Eds.; ICIRA 2022 Lecture Notes in Computer Science; Springer: Cham, Switzerland, 2022; Volume 13455, pp. 615–626. [CrossRef]
38. Lee, J.-H.; Chung, Y.S.; Rodrigue, H. Long Shape Memory Alloy Tendonbased Soft Robotic Actuators and Implementation as a Soft Gripper. *Sci. Rep.* **2019**, *9*, 11251. [CrossRef]
39. Guo, Z.; Pan, Y.; Wee, L.B.; Yua, H. Design and control of a novel compliant differential shape memory alloy actuator. *Sens. Actuator A-Phys.* **2015**, *225*, 71–80. [CrossRef]
40. Teodoriu, A.P.; Doroftei, I.; Pricop, B.; Bujoreanu, L.G. Study of the Load-Response Effect of NiTi-Based Thermal Actuators. Application to a Robotic Gripper. In *25th International Symposium on Measurements and Control in Robotics*; ISMCR 2023. Mechanisms and Machine Science; Doroftei, I., Kiss, B., Baudoin, Y., Taqvi, Z., Keller Fuchter, S., Eds.; Springer: Cham, Switzerland, 2024; Volume 154, pp. 237–251. [CrossRef]
41. Frenzel, J.; Wieczorek, A.; Opahle, I.; Maas, B.; Drautz, R.; Eggeler, G. On the effect of alloy composition on martensite start temperatures and latent heats in Ni–Ti-based shape memory alloys. *Acta Mater.* **2015**, *90*, 213–231.
42. Zhang, X.Y.; Sehitoglu, H. Crystallography of the B2→R→B 19′ phase transformations in NiTi. *Mater. Sci. Eng. A* **2004**, *374*, 292–302. [CrossRef]
43. Nam, T.H.; Saburi, T.; Shimizu, K. Cu-content dependence of shape memory characteristics in Ti-Ni-Cu alloys. *Mater. Trans. JIM* **1990**, *31*, 959–967. [CrossRef]

44. Wu, S.-K.; Lin, H.; Lin, T. Electrical resistivity of Ti–Ni binary and Ti–Ni–X (X = Fe, Cu) ternary shape memory alloys. *Mater. Sci. Eng. A* **2006**, *438–440*, 536–539. [CrossRef]
45. Harikrishnan, K.; Chandra, K.; Misra, P.S.; Agarwala Vinod, S. B19 orthorhombic martensitic transformations in aged TiNiCu shape memory alloys. In *ESOMAT 2009, Proceedings of the 8th European Symposium on Martensitic Transformations, Prague, Czech Republic, 7–11 September 2009*; Šittner, P., Heller, L., Paidar, V., Eds.; EDP Sciences: Les Ulis, France, 2009; p. 02020. [CrossRef]
46. Karthik, G.; Kashyap, B.; Ram Prabhu, T. Processing, properties and applications of Ni-Ti-Fe shape memory alloys. *Mater. Today Proc.* **2017**, *4*, 3581–3589. [CrossRef]
47. Kumar, A.; Palani, I.A.; Yadav, M. Comprehensive study of microstructure, phase transformations, and mechanical properties of nitinol alloys made of shape memory and superelastic wires and a novel approach to manufacture Belleville spring using wire arc additive manufacturing. *Mater. Today Commun.* **2024**, *38*, 107881. [CrossRef]
48. Li, X.C.; Su, Y. A phase-field study of the martensitic detwinning in NiTi shape memory alloys under tension or compression. *Acta Mech.* **2020**, *231*, 1539–1557. [CrossRef]
49. Isalgue, A.; Soul, H.; Yawny, A.; Auguet, C. Functional fatigue recovery of superelastic cycled NiTi wires based on near 100 °C aging treatments. In *ESOMAT 2015, Proceedings of the Tenth European Symposium on Martensitic Transformations, Antwerp, Belgium, 14–18 September 2015*; Schryvers, N., van Humbeeck, J., Eds.; EDP Sciences: Les Ulis, France, 2015; Volume 33, p. 03019. [CrossRef]
50. Delville, R.; Malard, B.; Pilch, J.; Sittner, P.; Schryvers, D. Transmission electron microscopy investigation of dislocation slip during superelastic cycling of Ni-Ti wires. *Int. J. Plasticity* **2011**, *27*, 282–297. [CrossRef]
51. Lohan, N.M.; Pricop, B.; Bujoreanu, L.-G.; Cimpoesu, N. Heating rate effects on reverse martensitic transformation in a Cu–Zn–Al shape memory alloy. *Int. J. Mater. Res.* **2011**, *102*, 1345–1351. [CrossRef]
52. Heller, L.; Sittner, P. On the habit planes between elastically distorted austenite and martensite in NiTi. *Acta Mater.* **2024**, *269*, 119828. [CrossRef]
53. Popa, M.; Lohan, N.-M.; Pricop, B.; Cimpoeșu, N.; Porcescu, M.; Comăneci, R.I.; Cazacu, M.; Borza, F.; Bujoreanu, L.-G. Structural-Functional Changes in a $Ti_{50}Ni_{45}Cu_5$ Alloy Caused by Training Procedures Based on Free-Recovery and Work-Generating Shape Memory Effect. *Nanomaterials* **2022**, *12*, 2088. [CrossRef] [PubMed]
54. Mihalache, E.; Pricop, B.; Comăneci, R.I.; Suru, M.-G.; Lohan, N.-M.; Mocanu, M.; Ozkal, B.; Bujoreanu, L.-G. Structural Effects of Thermomechanical Processing on the Static and Dynamic Responses of Powder Metallurgy Fe-Mn-Si Based Shape Memory Alloys. *Adv. Sci. Technol.* **2017**, *97*, 153–158.

Disclaimer/Publisher's Note: The statements, opinions and data contained in all publications are solely those of the individual author(s) and contributor(s) and not of MDPI and/or the editor(s). MDPI and/or the editor(s) disclaim responsibility for any injury to people or property resulting from any ideas, methods, instructions or products referred to in the content.